Revealing exciton transport in atomically thin semiconductors

Fengjiang Liu [1,2,*] Kai Chen,[3,4,5,*] Wei Yan,[1,2] Weiwei Tang,[1,2] Hao Zhang [3,4,6] Richard J. Blaikie,[3,4] Yu-Hui Chen,[7,†] Boyang Ding [3,4,6,8,‡] and Min Qiu[1,2,§]

[1]*School of Engineering, Westlake University, 18 Shilongshan Road, Hangzhou 310024, People's Republic of China*
[2]*Institute of Advanced Technology, Westlake Institute for Advanced Study, 18 Shilongshan Road, Hangzhou 310024, People's Republic of China*
[3]*Dodd-Walls Centre for Photonic and Quantum Technologies, Dunedin 9016, New Zealand*
[4]*MacDiarmid Institute for Advanced Materials and Nanotechnology, Wellington 6012, New Zealand*
[5]*Robinson Research Institute, Victoria University of Wellington, Wellington 6140, New Zealand*
[6]*Department of Physics, University of Otago, Dunedin 9016, New Zealand*
[7]*Key Laboratory of Advanced Optoelectronic Quantum Architecture and Measurements of Ministry of Education, Beijing Key Laboratory of Nanophotonics and Ultrafine Optoelectronic Systems, School of Physics, Beijing Institute of Technology, Beijing 10081, People's Republic of China*
[8]*Coherent Scientific Pty. Ltd., Thebarton, SA 5031, Australia*

(Received 9 September 2023; revised 16 January 2024; accepted 27 March 2024; published 14 May 2024)

Exciton transport is a fundamental process that underlies the functionality of semiconductor optoelectronic devices. However, when excitons interact with one another, their transport pattern becomes unpredictable, posing a great challenge to harness their full potential in various applications. In our study, focusing on the exciton density change in a tungsten-disulfide monolayer, we observed that strong interactions between excitons can actually stop their movement. This finding contradicts the typical understanding of consistent exciton movement and reveals that a higher density might decrease the exciton-exciton annihilation rate due to reduced mobility. Our findings offer a valuable technique to examine exciton transport and deepen our grasp of their behavior in many-body interactions, which could pave the way for better-performing excitonic devices.

DOI: 10.1103/PhysRevB.109.205418

I. INTRODUCTION

Exciton transport in semiconductors refers to the movement of bound electron-hole pairs from their generation origin to areas where they emit light or become free charge carriers. This process is crucial for numerous optoelectronic devices such as solar cells [1], photodetectors [2], and light-emitting diodes [3]. For these devices to function efficiently, excitons must reach specific regions for energy transfer, charge separation, or photon emission. As such, the efficiency and rate of exciton transportation exert a profound impact on the overall performance of optoelectronic devices [4,5].

However, exciton movement is significantly influenced by exciton-exciton interactions, e.g., Auger recombination (AR) and Coulomb forces. In AR, excitons within their interaction radius overlap in wave functions, leading to phonon production through Förster resonance energy transfer. Concurrently, Coulomb forces also act between exciton pairs, affecting their trajectories and energy states. Together, these interactions profoundly affect exciton behaviors such as annihilation, diffusion, and localization [6–13]. These effects are particularly pronounced in two-dimensional (2D) semiconductors, which sustain room-temperature excitons even at a confined space with atomically thin thicknesses [14–22], resulting in higher densities and stronger interactions. This amplifies the complexities of transport dynamics in 2D semiconductors, posing challenges for both fundamental understanding and practical applications [23–31].

In our study, we investigated the effects of exciton-exciton interactions on exciton mobility in tungsten-disulfide (WS_2) monolayers using transient absorption spectroscopy (TAS) [32]. We found that as exciton density approaches saturation, the diffusion coefficient significantly decreases, leading to nearly immobile excitons. This challenges established beliefs of a constant diffusion coefficient [2,33–36], typically observed under low-intensity excitations producing sparse exciton densities with minimal mobility impact [37,38]. Additionally, we discovered that the Auger recombination (AR) rate, indicating exciton annihilation, does not continually increase with higher exciton densities, challenging the prevalent view that higher densities always lead to accelerated AR rates [6,7]. Our findings provide valuable insights into exciton transport in 2D semiconductors, highlighting the complex influence of many-body effects on mobility and AR boundaries.

II. RESULTS

We studied these effects on a WS_2 monolayer that was grown on a sapphire substrate using chemical vapor deposition. Figure 1(a) shows the optical morphology of the WS_2

*These authors contributed equally to this work.
†stephen.chen@bit.edu.cn
‡boyang.ding@otago.ac.nz
§qiu_lab@westlake.edu.cn

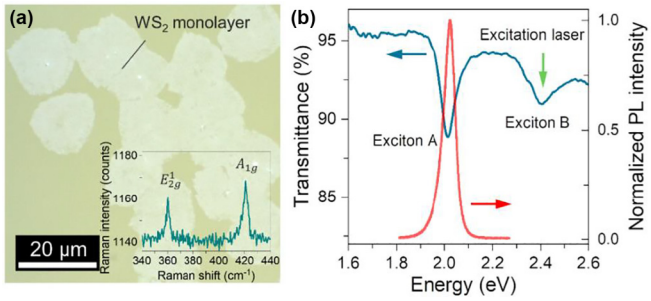

FIG. 1. Optical properties of WS_2 monolayer sample. (a) Optical morphology of WS_2 monolayer sample. The inset shows the Raman spectrum of the WS_2 monolayer, which exhibits two characteristic Raman peaks corresponding to the in-plane vibration E^1_{2g} and out-of-plane vibration A_{1g} modes. (b) Transmission and PL spectra of the WS_2 monolayer. The green arrow indicates the pump frequency (2.41 eV) of the transient absorption spectroscopy, which is located at the frequency of exciton B of WS_s monolayer. The PL spectrum in (b) is taken under a 2.33 eV (532 nm) excitation with a power of 0.1 mW.

monolayer sample, which exhibits discrete islands of WS_2 flakes with typical diameter of ∼20 μm. The monolayer character of the WS_2 flakes is identified by Raman, transmission, and photoluminescence (PL) spectroscopy, as shown in the inset of Figs. 1(a) and 1(b). The transmission spectrum of the WS_2 monolayer is shown in Fig. 1(b), which exhibits two resonance peaks at 2.014 and 2.403 eV, corresponding to the direct A/B excitonic transitions. Under low-power cw laser excitation, the photoluminescence (PL) spectrum is centered around the exciton-A resonance [Fig. 1(b)].

Our exploration begins with an assessment of the injected density of excitons. Specifically, we use a pulsed laser with a frequency of 2.41 eV to optically pump the sample. This excitation generates electron-hole pairs at the exciton-B (X_B) frequency of WS_2, as illustrated in Fig. 1. In an ultrashort span, approximately 100 fs, these pairs experience rapid relaxation, descending to the exciton-A (X_A) state around 2.0 eV. Once formed, these X_A excitons undergo spontaneous relaxation and AR annihilation, causing a decline in their densities. Thus, monitoring the density fluctuations of X_A over time offers valuable insights into the dynamics of exciton decay and their mutual interactions. It is worth noting that in this paper, any mention of "exciton" refers to X_A unless specified differently.

In our experiments, we observed that the ratio of transmitted to incident pump power remains stable as the pump fluence rises, confirming consistent absorbance in the studied range of our TAS measurements. This consistent absorption behavior of the WS_2 monolayer at the frequency of 2.41 eV with escalating pump fluences allows us to directly calculate the injected density of X_A. Specifically, as the quantum numbers of excitons remain conserved in the X_B-to-X_A conversion [39], we can correlate injected X_A densities with pump fluences. This was achieved by utilizing the equation $N_0 = FA/(\hbar\omega)$. In this equation, F represents the pump fluence, $\hbar\omega$ signifies the energy of the pump photon, and $A = 3.3\%$, derived from the transmittance of the WS_2 monolayer at the pump frequency, stands for the absorption

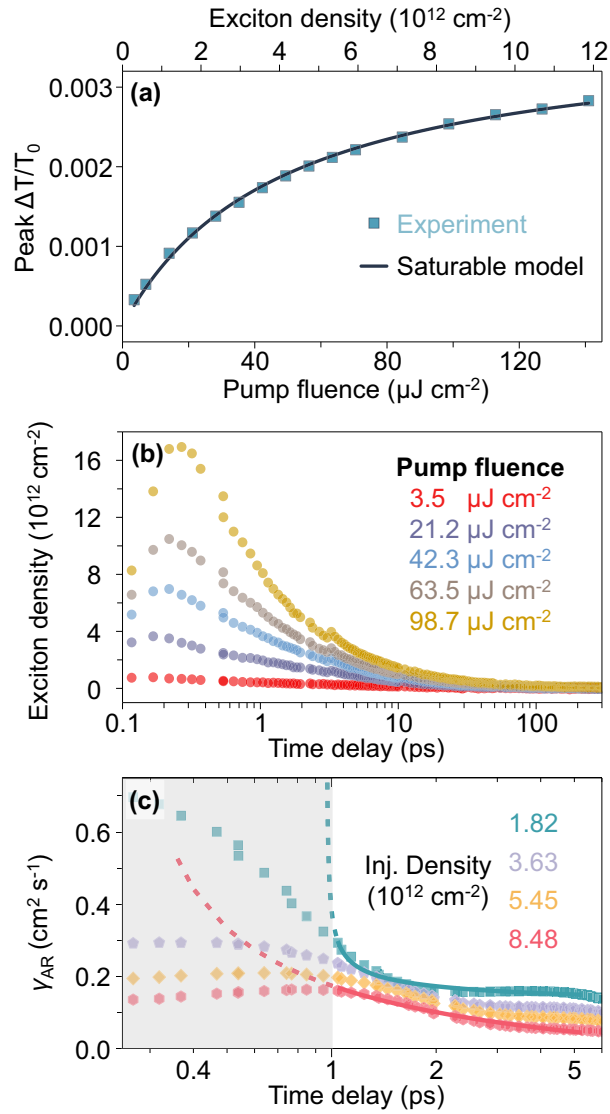

FIG. 2. Time-dependent exciton density change. (a) Pump fluence (injected exciton density)-dependent peak $\Delta T/T_0$ and the fitting using a saturable model Eq. (1). (b) Exciton density decays for five different injected exciton densities as noted. (c) $\gamma_{AR}(t)$ (solid squares) obtained by fitting the decay of $n(t)$ with different injected densities using Eq. (2); $\gamma_{AR}(t)$ (dashed curves) obtained by fitting $n(t)$ using both Eqs. (2) and (3) with diffusion coefficients D being set as constants. In both fittings, $\tau_X = 11.1$ ps is the lifetime of a singlet exciton without exciton-exciton interactions.

coefficient. These are marked on the upper and lower x axes of Fig. 2(a).

Once we have obtained the injected densities, we can measure density change during decay process using optical pump-probe spectroscopy. In particular, the presence of X_A indicates the occupation of excitonic states, which means the number of available states for subsequent optical excitation is reduced. In other words, optically pumping a WS_2 monolayer decreases its absorption for later arriving photons. Hence, by employing a light beam to probe the semiconductor at a delay of t after pumping, we can monitor the time-dependent exciton density $n(t)$. This is obtained by comparing

the transmission of the probe beam with pumping (T) and without pumping (T_0), i.e., the time-dependent differential transmission $\Delta T/T_0 = (T - T_0)/T_0$ at the frequency of X_A. Figure 2(a) illustrates the maximum values of $\Delta T/T_0$ under different injected densities, establishing a correlation between the transient absorption signal and a specific exciton density. It is evident that $\Delta T/T_0$ follows a saturable model [28]:

$$\frac{\Delta T}{T_0} \propto \frac{n(t)}{n(t) + N_s}. \tag{1}$$

Here, the exciton saturation density N_s represents the density at which excitons are closely packed in the 2D plane of the WS_2 monolayer. By fitting the $\Delta T/T_0$ values from different pump fluences in Fig. 2(a) using Eq. (1), we find $N_s = (4.1 \pm 0.3) \times 10^{12}$ cm^{-2}. Importantly, this saturation density remains below the Mott transition threshold, avoiding exciton dissociation into free carriers [34,40]. Our approach effectively translates measured $\Delta T/T_0$ signals into exciton densities, providing valuable insights for understanding the relaxation process [28].

Figure 2(b) distinctly illustrates the change in exciton density over time under varying pump fluences. The decay of excitons primarily arises from two mechanisms: (i) the inherent relaxation of individual excitons, with a measured lifetime $\tau_X = 11.1$ ps derived from low-pump-intensity TAS experiments, and (ii) the AR annihilation, whose rate is thought to be heavily influenced by exciton density, given that AR stems from interactions between excitons. Here, we delve deeper into this process. The decay of exciton can be described by a rate equation [2,33–35],

$$\frac{dn(t)}{dt} = -\frac{1}{\tau_X} n(t) - \frac{1}{2}\gamma_{AR}(t) n^2(t), \tag{2}$$

where the coefficient $\gamma_{AR}(t)$ determines the rate of AR annihilation. Using Eq. (2) to analyze the density curves from Fig. 2(b), we established the temporal behavior of $\gamma_{AR}(t)$ across varying injection densities, depicted as solid squares in Fig. 2(c). Clearly, γ_{AR} changes over time: It decays for $t > 1$ ps, indicating a diminishing AR process, but for $t < 1$ ps, its behavior is strongly influenced by pump fluences. Specifically, higher densities tend to decrease the magnitude of γ_{AR}.

To investigate the complex variation of γ_{AR}, we further analyzed its determinants. Specifically, in 2D materials, γ_{AR} can be expressed as [41,42]

$$\gamma_{AR}(t) = \frac{8DR}{\pi} \int_0^\infty \frac{e^{-Du^2 t}}{u\left[J_0^2(uR) + Y_0^2(uR)\right]} du, \tag{3}$$

where R signifies the singlet exciton's interaction radius, and D denotes its diffusion coefficient, indicating how fast excitons can move within a 2D lattice, and J_0 and Y_0 are the first and second kind zero-order Bessel functions, respectively.

It is evident that γ_{AR} is closely tied to R and D. Our results show that R remains stable after time delay of $t >$ 0.4 ps. Specifically, when excitons are initially formed, they can appear in high-energy Rydberg states with excess kinetic energy, which manifest large interaction radii R. However, an increased R suggests that these excitons interact strongly with their environment, making this expanded R lasts for only ~100 fs. Subsequently, excitons transition to the 1s Rydberg ground state within the initial 0.3 ps, as shown in Fig. 2(b) and corroborated by recent research [43].

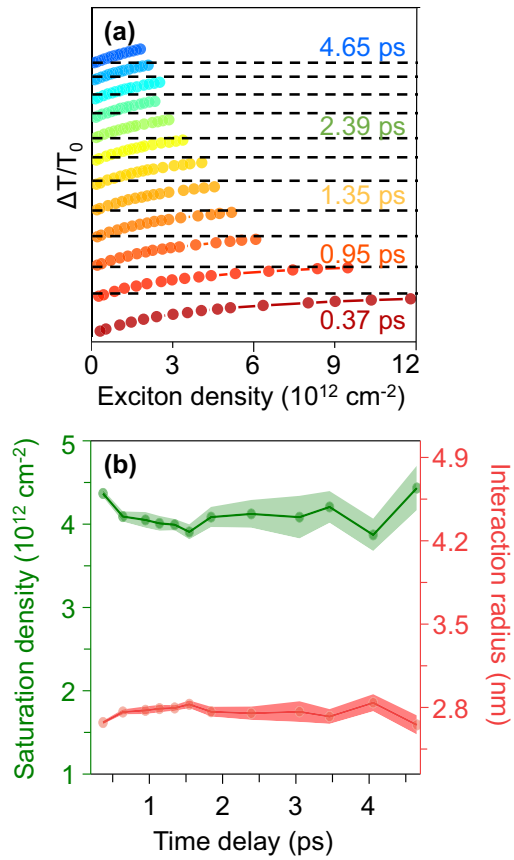

FIG. 3. Temporally resolved effective exciton interaction radius. (a) The dependence of $\Delta T/T_0$ on the injected exciton density for different time delays, i.e., the $\Delta T(\tau_d + 0.1\ \text{ps})/T_0$ as a function of the exciton density at the moment τ_d. The solid lines are fittings using the saturable model Eq. (1). (b) Dependence of saturation density (green curve) and interation radius (red curve) on time. The data points are extracted from (a).

The interaction radius R for delays exceeding 0.3 ps can be derived by analyzing saturation densities. The curve in Fig. 2(a) links $\Delta T/T_0$ with exciton densities. This relationship is consistent in Fig. 3(a), where $\Delta T/T_0$ values correspond with Eq. (1) post 0.3 ps. From this, we identified saturated densities N_s at different delays [in Fig. 3(b)]. Recognizing N_s depicts a densely packed exciton scenario, we calculated R using $N_s = \pi R^2$. Presented in Fig. 3(b), there is a stable interaction radius of ~2.8 nm, aligning with models [44–46] and experiments [39,47–50] on 2D semiconductors, suggesting a 1–2 nm exciton size and 3–4 nm interaction radius. These findings indicate that the interaction distance is within the Förster energy transfer's effective range. While the Dexter-type process might also be involved, its impact on AR annihilation, primarily driven by Förster energy transfer, appears minimal. Further exploration of the Dexter-type process's role, as suggested in Ref. [4], is needed but falls outside this study's scope.

Given that the interaction radius R is consistent over time, the primary factor affecting $\gamma_{AR}(t)$ becomes the exciton

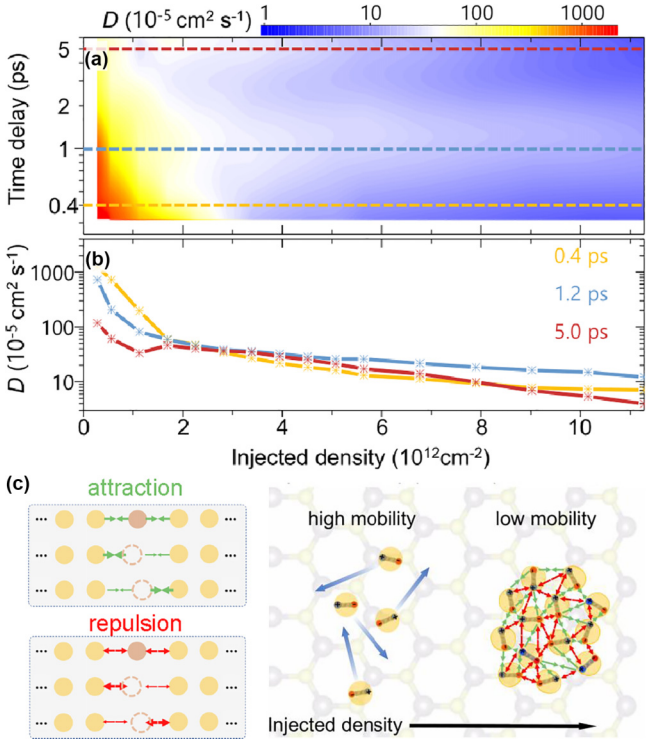

FIG. 4. Mobility influenced by exciton-exciton interactions. (a) Exciton mobility (D) over time at different exciton densities, with time delays marked by red (5 ps), blue (1.2 ps), and orange (0.4 ps) dashed lines. (b) Exciton mobility correlated with various exciton densities at specific delay times indicated in (a). (c) Diagram showing exciton attraction and repulsion, highlighting decreased mobility due to increased exciton-exciton interactions at high densities.

diffusion coefficient D. Using Eqs. (2) and (3), we fitted the density curves from Fig. 2(c) to extract $D(t)$, as depicted in Fig. 4(a). For this fit, we converted the unit of exciton density $n(t)$ from cm^{-2} to cm^{-3} by assuming a 1 nm monolayer thickness [14].

We observe significant temporal variations in D. At low injected densities below 2.1×10^{12} cm^{-2}, the diffusion coefficient D decreases over time. This decline aligns with the Einstein relation $D = \mu k_B T$, where μ corresponds to $1/m\kappa$, m is the exciton's effective mass, and κ is its phonon interaction rate. After optical excitation, the elevated exciton temperature inflates D. As they cool, losing kinetic energy [51], D falls sharply.

As the injected density rises, D's temporal behavior becomes intricate, not solely attributed to diminishing processes. The impact of exciton-exciton interactions is evident. As depicted in Fig. 4(b), a higher density notably reduces exciton mobility D. For example, at 0.4 ps, D drops drastically with density elevation, nearing zero at 5 ps for high densities, suggesting excitons behave more as a solid than a bosonic gas due to exciton-exciton interactions.

III. DISCUSSION

The influence of injected density on exciton mobility, to the best of our knowledge, remains unreported. This oversight likely stems from the fact that established principles of exciton transport are based on three-dimensional (3D) bulk semiconductors. In 3D systems, the exciton density is not dense enough to trigger impactful exciton-exciton interactions. In contrast, 2D semiconductors, due to their reduced dimensionality, have a heightened exciton density, leading to intensified exciton-exciton interactions [52,53].

When exciton interactions are considered, they can exert driving or fictitious forces that either enhance or hinder exciton mobility. Describing the dynamics involves complex interconnected degrees of freedom [54–58]. A mesoscopic approach, which incorporates the concept of local equilibrium [55], allows for the calculation of the local system entropy and identification of forces in a similar manner to irreversible thermodynamics. Assuming that interactions only occur between two-body pairs, the mobility affected by interaction potential $\phi(r)$ is [55]

$$D = \mu k_B T \left[1 - \frac{4}{3}\pi \frac{n(t)}{k_B T m} \int_0^\infty \frac{\partial \phi(r)}{\partial r} g^{(2)}(r) r^3 dr \right], \quad (4)$$

where $n(t)$ is the density of excitons, $\phi(\mathbf{r_2} - \mathbf{r_1}) = \phi(r)$ is the interaction potential between two excitons at positions $\mathbf{r_1}$ and $\mathbf{r_2}$, which depends solely on the distance between the excitons, and $g^{(2)}(r)$ is the correlation function of two excitons and is also only dependent on distance.

The impact of many-body interactions on exciton mobility is determined by whether the potential $\phi(r)$ exerts an attractive or repulsive force, as illustrated in Fig. 4(c). In the case of attractive forces, when an exciton is displaced from its equilibrium position, the attractive forces act to drive the exciton further in the same direction. Conversely, in the case of repulsive forces, when an exciton attempts to move towards its neighboring exciton, the repulsive forces impede its motion, acting as a barrier that opposes the motion of the exciton. Precisely characterizing exciton interactions is a complex undertaking [59]. However, for simple repulsive interaction potentials [54,55], the mobility of interacting excitons can be evaluated using the following expression,

$$D = \mu k_B T (1 - 2f), \quad (5)$$

where $f \propto n$ is the volume fraction of the excitons. This equation shows that the mobility generally experiences a decrease as the density rises.

Drawing on an exciton-exciton interaction model [53], we propose a pivotal role for Coulomb interactions between excitons in diminishing exciton mobility at elevated densities. Excitons, being electron-hole pairs, inherently engage in Coulombic interactions with other excitons. These interactions present as attraction or repulsion based on their relative orientations [Fig. 4(c)]. With increasing density, excitons tend to concentrate and eventually reach a saturation point. This marks a threshold where repulsive Coulomb forces outweigh the attractive forces, hindering further compression of excitons. Additionally, each exciton is encircled by a similar number of counterparts, which collectively exert a counterforce, impeding the movement of individual excitons. This results in a notable decrease in overall exciton mobility.

As a result, exciton-exciton interactions introduce complexity in the temporal behavior of a diffusion coefficient. While the Einstein relation suggests that exciton decay

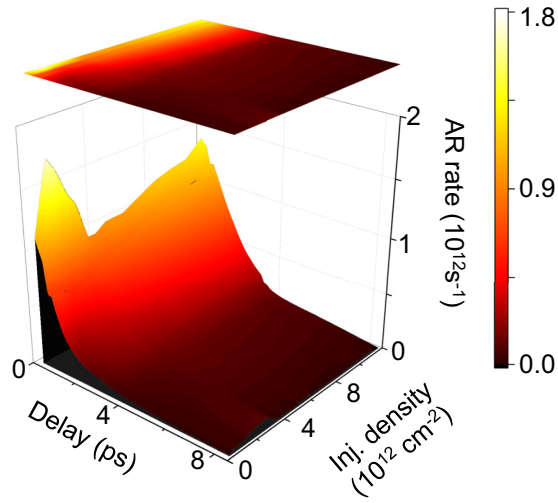

FIG. 5. AR annihilation rate for different injected exciton densities. The product of $\gamma_{AR}(t) \cdot n(t)/2$ is plotted as a function of time delay and injected exciton densities. The AR rate peaks at 1.9×10^{12} cm^{-2} and stabilizes at 4.1×10^{12} cm^{-2}.

leads to cooling, thus reducing mobility, exciton relaxation concurrently decreases many-body interactions, potentially increasing mobility. This interplay manifests distinctly in $D(t)$. For instance, as shown in Fig. 4(a), at high injected densities, $D(t)$ peaks not immediately but around 1 ps after some decay. This is more pronounced in Fig. 4(b), where for densities above 6×10^{12} cm^{-2}, the peak diffusion occurs at 1.2 ps, indicating a balance between cooling effects and reduced many-body interactions.

According to Eq. (3), the complex exciton mobility due to exciton-exciton interactions directly influences the AR coefficient $\gamma_{AR}(t)$. This accounts for the counterintuitive behavior seen in Fig. 2(c), where a higher injected density surprisingly results in a reduced γ_{AR}. In contrast, using constant D values in Eqs. (2) and (3) can yield notably different γ_{AR}, particularly for $t < 1$ ps, as indicated by the dashed curves in Fig. 2(c). This confirms the complexity of exciton mobility.

The AR annihilation rate, expressed as $\gamma_{AR}(t) \cdot n(t)/2$, challenges the traditional belief that annihilation rate simply increases with exciton density. Our findings indicate that this rate is maximal at an injected density of $N_{th} = 1.9 \times 10^{12}$ cm^{-2} at $t = 0.3$ ps, as depicted in Fig. 5. While higher injection increases $n(t)$, they concurrently decrease $D(t)$, thereby constraining exciton annihilation. This results from the delicate interplay between density and mobility, causing the AR annihilation rate to peak at a specific exciton density.

Beyond a density of $N_{th} = 1.9 \times 10^{12}$, the rate drops significantly due to diminished exciton mobility. When the density surpasses $N_{th} = 4.1 \times 10^{12}$ cm^{-2}, AR rates stabilize, with only minor increases as density continues to rise. At such high densities, additional excitons do not substantially affect collision probabilities. The reduced annihilation rate is due to the dynamic balance between exciton density and mobility. While a higher exciton density theoretically increases annihilation probability due to greater spatial overlap, it simultaneously decreases mobility, reducing the encounter possibility between excitons and thus lowering annihilation rates. This illustrates the complex interplay among exciton density, mobility, and interaction likelihood. Understanding this behavior is crucial for high-speed excitonic devices, since maintaining lower AR rates during the initial relaxation phase can enhance their performance and longevity.

Despite variations in band structure, dielectric screening, and other material-specific characteristics, the core principles of exciton interactions remain consistent across different 2D materials. Notably, when exciton density nears saturation, causing excitons to pack closely, repulsion becomes the dominant force, limiting their mobility. Thus, while our study's insights on exciton-exciton interactions and mobility are specific to WS_2 monolayers, the fundamental concepts are applicable to other 2D materials as well.

IV. CONCLUSION

In summary, through pump-probe spectroscopy, we explored exciton mobility in a WS_2 monolayer. Our analysis of temporal exciton density changes revealed a balance between exciton density and mobility. While low densities showcased high exciton mobility, increased densities intensified exciton-exciton interactions, thereby limiting their diffusion and reducing mobility. This interplay eventually led excitons to solidify, decreasing AR annihilation rates. This research illuminates fundamental exciton dynamics in 2D semiconductors and introduces an efficient method to study exciton transport in such materials.

ACKNOWLEDGMENTS

This work was supported in part by the National Key Research and Development Program of China (No. 2017YFA0205700) and the National Natural Science Foundation of China (No. 12174026, No. 12004311, No. 62105033, No. 61425023, No. 61235007, and No. 61575177). In addition, the authors acknowledge the New Idea Research Funding 2018 (Dodd-Walls Centre for photonic and quantum technologies) and Smart Ideas Funds 2018 by MBIE New Zealand.

[1] S. M. Menke and R. J. Holmes, Energy Environ. Sci. **7**, 499 (2014).
[2] O. V. Mikhnenko, P. W. M. Blom, and T.-Q. Nguyen, Energy Environ. Sci. **8**, 1867 (2015).
[3] S. Reineke, F. Lindner, G. Schwartz, N. Seidler, K. Walzer, B. Lüssem, and K. Leo, Nature (London) **459**, 234 (2009).
[4] A. J. Sneyd, D. Beljonne, and A. Rao, J. Phys. Chem. Lett. **13**, 6820 (2022).
[5] S. Chandrabose, K. Chen, A. J. Barker, J. J. Sutton, S. K. Prasad, J. Zhu, J. Zhou, K. C. Gordon, Z. Xie, X. Zhan, and J. M. Hodgkiss, J. Am. Chem. Soc. **141**, 6922 (2019).
[6] L. Yuan, T. Wang, T. Zhu, M. Zhou, and L. Huang, J. Phys. Chem. Lett. **8**, 3371 (2017).

[7] G. Wang, A. Chernikov, M. M. Glazov, T. F. Heinz, X. Marie, T. Amand, and B. Urbaszek, Rev. Mod. Phys. **90**, 021001 (2018).

[8] S. Z. Uddin, H. Kim, M. Lorenzon, M. Yeh, D.-H. Lien, E. S. Barnard, H. Htoon, A. Weber-Bargioni, and A. Javey, ACS Nano **14**, 13433 (2020).

[9] C. Cong, J. Shang, Y. Wang, and T. Yu, Adv. Opt. Mater. **6**, 1700767 (2018).

[10] F. Ceballos, Q. N. Cui, M. Z. Bellus, and H. Zhao, Nanoscale **8**, 11681 (2016).

[11] Z. Sun, A. Ciarrocchi, F. Tagarelli, J. F. Gonzalez Marin, K. Watanabe, T. Taniguchi, and A. Kis, Nat. Photonics **16**, 79 (2022).

[12] S. Deng, E. Shi, L. Yuan, L. Jin, L. Dou, and L. Huang, Nat. Commun. **11**, 664 (2020).

[13] V. Pareek, J. Madéo, and K. M. Dani, Phys. Rev. Lett. **124**, 057403 (2020).

[14] F. Xia, H. Wang, D. Xiao, M. Dubey, and A. Ramasubramaniam, Nat. Photonics **8**, 899 (2014).

[15] H. Zeng and X. Cui, Chem. Soc. Rev. **44**, 2629 (2015).

[16] K. F. Mak and J. Shan, Nat. Photonics **10**, 216 (2016).

[17] R. J. P. Román, Y. Auad, L. Grasso, F. Alvarez, I. D. Barcelos, and L. F. Zagonel, Nanoscale **12**, 13460 (2020).

[18] J. H. Chen, J. Tan, G. X. Wu, X. J. Zhang, F. Xu, and Y. Q. Lu, Light: Sci. Appl. **8** (2019).

[19] H. Wang, C. Zhang, W. Chan, S. Tiwari, and F. Rana, Nat. Commun. **6**, 8831 (2015).

[20] I. Datta, S. H. Chae, G. R. Bhatt, M. A. Tadayon, B. Li, Y. Yu, C. Park, J. Park, L. Cao, D. N. Basov, J. Hone, and M. Lipson, Nat. Photonics **14**, 256 (2020).

[21] D. Deng, K. S. Novoselov, Q. Fu, N. Zheng, Z. Tian, and X. Bao, Nat. Nanotechnol. **11**, 218 (2016).

[22] X. Yu, M. S. Prévot, N. Guijarro, and K. Sivula, Nat. Commun. **6**, 7596 (2015).

[23] P. D. Cunningham, K. M. McCreary, and B. T. Jonker, J. Phys. Chem. Lett. **7**, 5242 (2016).

[24] H. J. Shin, S. Bae, and S. Sim, Nanoscale **12**, 22185 (2020).

[25] M. Kulig, J. Zipfel, P. Nagler, S. Blanter, C. Schüller, T. Korn, N. Paradiso, M. M. Glazov, and A. Chernikov, Phys. Rev. Lett. **120**, 207401 (2018).

[26] D. Sun, Y. Rao, G. A. Reider, G. Chen, Y. You, L. Brézin, A. R. Harutyunyan, and T. F. Heinz, Nano Lett. **14**, 5625 (2014).

[27] L. Yuan and L. Huang, Nanoscale **7**, 7402 (2015).

[28] N. Kumar, Q. Cui, F. Ceballos, D. He, Y. Wang, and H. Zhao, Phys. Rev. B **89**, 125427 (2014).

[29] Y. Yu, Y. Yu, C. Xu, A. Barrette, K. Gundogdu, and L. Cao, Phys. Rev. B **93**, 201111 (2016).

[30] S. Mouri, Y. Miyauchi, M. Toh, W. Zhao, G. Eda, and K. Matsuda, Phys. Rev. B **90**, 155449 (2014).

[31] Y. Li, J. Shi, Y. Mi, X. Sui, H. Xu, and X. Liu, J. Mater. Chem. C **7**, 4304 (2019).

[32] J. Dostál, F. Fennel, F. Koch, S. Herbst, F. Würthner, and T. Brixner, Nat. Commun. **9**, 2466 (2018).

[33] D. Rais, M. Menšík, B. Paruzel, P. Toman, and J. Pfleger, J. Phys. Chem. C **122**, 22876 (2018).

[34] P. E. Shaw, A. Ruseckas, J. Peet, G. C. Bazan, and I. D. W. Samuel, Adv. Funct. Mater. **20**, 155 (2010).

[35] X.-H. Jin, M. B. Price, J. R. Finnegan, C. E. Boott, J. M. Richter, A. Rao, S. M. Menke, R. H. Friend, G. R. Whittell, and I. Manners, Science **360**, 897 (2018).

[36] Y. Tamai, Y. Matsuura, H. Ohkita, H. Benten, and S. Ito, J. Phys. Chem. Lett. **5**, 399 (2014).

[37] K. J. Lee, W. Xin, and C. Guo, Phys. Rev. B **101**, 195407 (2020).

[38] T. Zhang, C. Zhou, J. Lin, and J. Wang, ACS Photonics **9**, 1627 (2022).

[39] A. Chernikov, C. Ruppert, H. M. Hill, A. F. Rigosi, and T. F. Heinz, Nat. Photonics **9**, 466 (2015).

[40] D. P. Khatua, A. Singh, S. Gurung, S. Khan, M. Tanwar, R. Kumar, and J. Jayabalan, J. Phys.: Condens. Matter **34**, 155401 (2022).

[41] K. Razi Naqvi, Chem. Phys. Lett. **28**, 280 (1974).

[42] H. Ohkita, Y. Tamai, H. Benten, and S. Ito, IEEE J. Sel. Top. Quantum Electron. **22**, 100 (2016).

[43] C. Trovatello, F. Katsch, N. J. Borys, M. Selig, K. Yao, R. Borrego-Varillas, F. Scotognella, I. Kriegel, A. Yan, A. Zettl, P. J. Schuck, A. Knorr, G. Cerullo, and S. D. Conte, Nat. Commun. **11**, 5277 (2020).

[44] J. Zipfel, J. Holler, A. A. Mitioglu, M. V. Ballottin, P. Nagler, A. V. Stier, T. Taniguchi, K. Watanabe, S. A. Crooker, P. C. M. Christianen, T. Korn, and A. Chernikov, Phys. Rev. B **98**, 075438 (2018).

[45] T. C. Berkelbach, M. S. Hybertsen, and D. R. Reichman, Phys. Rev. B **88**, 045318 (2013).

[46] R.-Z. Li, X.-Y. Dong, Z.-Q. Li, and Z.-W. Wang, Solid State Commun. **275**, 53 (2018).

[47] M. Goryca, J. Li, A. V. Stier, T. Taniguchi, K. Watanabe, E. Courtade, S. Shree, C. Robert, B. Urbaszek, X. Marie, and S. A. Crooker, Nat. Commun. **10**, 4172 (2019).

[48] M. K. Man, J. Madéo, C. Sahoo, K. Xie, M. Campbell, V. Pareek, A. Karmakar, E. L. Wong, A. Al-Mahboob, N. S. Chan, D. R. Bacon, X. Zhu, M. M. Abdelrasoul, X. Li, T. F. Heinz, F. H. D. Jornada, T. Cao, and K. M. Dani, Sci. Adv. **7**, eabg0192 (2021).

[49] A. V. Stier, N. P. Wilson, K. A. Velizhanin, J. Kono, X. Xu, and S. A. Crooker, Phys. Rev. Lett. **120**, 057405 (2018).

[50] T. Kato and T. Kaneko, ACS Nano **10**, 9687 (2016).

[51] C. Ruppert, A. Chernikov, H. M. Hill, A. F. Rigosi, and T. F. Heinz, Nano Lett. **17**, 644 (2017).

[52] A. W. Achtstein, S. Ayari, S. Helmrich, M. T. Quick, N. Owschimikow, S. Jaziri, and U. Woggon, Nanoscale **12**, 23521 (2020).

[53] D. Erkensten, S. Brem, and E. Malic, Phys. Rev. B **103**, 045426 (2021).

[54] H. N. W. Lekkerkerker and J. K. G. Dhont, J. Chem. Phys. **80**, 5790 (1984).

[55] M. Mayorga, L. Romero-Salazar, and J. Rubi, Physica A **307**, 297 (2002).

[56] M. Krüger and M. Fuchs, Prog. Theor. Phys. Suppl. **184**, 172 (2010).

[57] B. U. Felderhof, J. Phys. A: Math. Gen. **11**, 929 (1978).

[58] T. J. Murphy and J. L. Aguirre, J. Chem. Phys. **57**, 2098 (1972).

[59] P. Geiregat, A. Houtepen, Y. Justo, F. C. Grozema, D. Van Thourhout, and Z. Hens, J. Phys. Chem. C **118**, 22284 (2014).